JGR | Machine Learning and Computation

RESEARCH ARTICLE
10.1029/2025JH000906

Surfzone Water Depth Estimation From Surface Flows Using a Data-Driven and Physics-Informed Deep Conditional Generative Model

Reza Salatin[1,2], **Steve Elgar**[1], **and Britt Raubenheimer**[1]

[1]Woods Hole Oceanographic Institution, Woods Hole, MA, USA, [2]Northeastern University, Boston, MA, USA

Key Points:

- A deep conditional generative model encodes surface flows into a latent space for estimating surfzone water depths (bathymetry)
- The model estimates surfzone water depths on non-survey days, enabling continuous monitoring
- This method has potential to reduce the need for frequent, expensive in situ bathymetric surveys

Correspondence to:
S. Elgar,
elgar@whoi.edu

Citation:
Salatin, R., Elgar, S., & Raubenheimer, B. (2026). Surfzone water depth estimation from surface flows using a data-driven and physics-informed deep conditional generative model. *Journal of Geophysical Research: Machine Learning and Computation*, *3*, e2025JH000906. https://doi.org/10.1029/2025JH000906

Received 21 JUL 2025
Accepted 22 DEC 2025

Abstract A physics-informed deep conditional generative model driven with remotely sensed surface currents is shown to estimate surfzone water depths (bathymetry). The model encodes measured flow data as latent Gaussian parameters and decodes these distributions to estimate water depths over the domain, progressively refining its predictions via a loss-minimization strategy. The model performance is evaluated on in-distribution and out-of-distribution data sets collected in Duck, North Carolina, demonstrating promising site-specific results, especially given the limited training data set used here (6 bathymetries with a total of 8 flow realizations). However, broader applicability requires transfer learning across a wider range of bathymetric observations.

Plain Language Summary Irregularities in the seafloor near the shoreline (including curving sandbars, channels, bumps, and holes) cause spatial variations in waves approaching the coast, which can result in strong and variable flows parallel (alongshore currents) and perpendicular (rip currents) to the beach. Thus, having a map of the seafloor is important to predict the wave-driven flow patterns and the corresponding transport of pollution, biota, sediment, and swimmers from the beach to deeper water. However, obtaining accurate maps of the seafloor is difficult in areas with breaking waves (the surfzone). For safety, surveying with vessels is limited to calm conditions. However, the bottom changes during both mild conditions and storms, and thus the surveyed maps typically are accurate for only a few days. Here, surfzone flows estimated by tracking breaking-wave-generated foam in video images are input to an artificial intelligence system that estimates the underlying seafloor shape (bathymetry). Although the data set used for training is limited, the results suggest that this approach may provide estimates of the surfzone bathymetry during a wide range of wave conditions.

1. Introduction

Surfzone morpho- and hydrodynamics are critical to storm impacts along the coast, as well as beach recovery following storms (Sallenger, 2000; Sallenger et al., 2004, 2005, 2006, 2007). Alongshore undulations in surfzone bathymetry affect wave energy reaching the shore via variable dissipation and focusing, modulate the strength and position of strong offshore-directed "rip" currents, and affect rates of shoreline recovery (Castelle et al., 2017; MacMahan et al., 2006; Phillips, Brown, et al., 2017; Thornton et al., 2007). Storms often trigger changes in alongshore beach morphological patterns (Lippmann & Holman, 1990; Ruessink et al., 2007; Wright & Short, 1984), but the relative importance of hydrodynamic forcing, antecedent sandbar and shoreline configuration, and feedbacks between morphology and surfzone circulation remain uncertain. Post-storm shoreward movement of sandbars may contribute to beach recovery, with onshore migration rates depending on alongshore variability, sandbar shapes, and preceding wave conditions (Phillips, Harley, et al., 2017; Vidal-Ruiz & de Alegría-Arzaburu, 2020). Understanding how the morphologic-hydrodynamic system varies along the coast during and following storms is essential for informing coastal management decisions (de Swart et al., 2021; Di Leonardo & Ruggiero, 2015). Obtaining accurate bathymetry is recognized as one of the most significant limitations in understanding nearshore processes, especially during storms (Salim & Wilson, 2021; Van Dongeren et al., 2008).

Although sandbar behavior has been inferred from time-averaged images of breaking wave foam, these techniques do not produce depth profiles and are sensitive to changes in mean water levels (tides and surge) and wave heights (Guedes et al., 2011; Lippmann & Holman, 1990; Plant & Holman, 1999; Ruessink et al., 2009; Van Enckevort & Ruessink, 2001). Time-averaged foam patterns provide qualitative evidence that the initial transition of sandbars from linear to alongshore variable may occur rapidly as wave energy decreases, but that continued

periods of low wave energy are needed for large-scale 3-dimensional bathymetric features to form (Lippmann & Holman, 1990). The averaged foam patterns from which rapid evolution is inferred may not reflect the underlying seafloor features (Van Enckevort & Ruessink, 2001), especially during storms when waves are breaking in a wide range of depths.

Conventional survey methods using sensors mounted on manned or autonomous surface vessels (Dugan et al., 2001; Francis & Traykovski, 2021; Ruggiero et al., 2005) or bottom crawlers (Birkemeier & Mason, 1984) are expensive and are not possible during the large breaking waves and strong currents in storms. Airborne LiDAR maps nearshore regional bathymetry, but may be inaccurate in shallow areas with significant wave breaking (foam) or suspended sediments, and often does not resolve 100-m scale features owing to incomplete spatial coverage from limited water penetration and interpolation artifacts introduced when filling data gaps (Janowski et al., 2022; Robertson et al., 2018). Bathymetry also has been estimated indirectly using surface wave propagation measured with optical cameras (Holman et al., 2013), LiDAR (Blenkinsopp et al., 2012; Brodie et al., 2015; Martins et al., 2025; Wilson & Berezhnoy, 2018), radar (Haller et al., 2014), and infrared (Dugan et al., 1996). Algorithms such as cBathy (Brodie et al., 2018; Holman & Bergsma, 2021; Holman et al., 2013; Honegger et al., 2019; Lange et al., 2023; O'Dea et al., 2025) have skill mapping sandbars during mild wave conditions (wave heights of ∼1 m or less), but are less accurate for energetic waves during storms, when air- and space-based sensors, as well as oblique land-based systems, can be hindered by atmospheric conditions. Clouds, fog, heavy rain, or sea-spray can obscure optical and IR imagery, and strong winds can prevent drones from flying, making it especially difficult to collect data when energetic waves are most important (Lillesand et al., 2015). Consequently, most investigations of nearshore processes depend on bathymetric surveys obtained before and after storms, numerical simulations, or behavior inferred from averaged foam patterns.

Inverse and data assimilation techniques (Birrien et al., 2013; Lewis et al., 2006; Wilson et al., 2014; Wu et al., 2023) and artificial intelligence methods (Adusumilli et al., 2024; Chen et al., 2023; Collins et al., 2020, 2021; Ellenson et al., 2020; Lowell & Calder, 2021; Salatin et al., 2024; Wang et al., 2022) have shown promise for estimating nearshore processes given numerical model output and data from spatially sparse in situ sensors, or time averaged images of breaking-wave foam. Recent deep learning techniques, including fully convolutional networks, have been used to estimate coastal inundation depths from community-contributed images and videos (Kabir et al., 2020; Liang et al., 2023; Muñoz et al., 2021), high coastal water levels (Palmer et al., 2024), swash motion in rapid image sequences to enhance understanding of alongshore variability in wave runup on sandy beaches (Salatin et al., 2024), and nearshore bathymetry by leveraging optical indicators of wave dynamics, such as time-averaged images and single-frame image inputs (Collins et al., 2020).

Surface flow maps provided by remote sensing enable new techniques for estimating surfzone bathymetry. Specifically, advances in particle image velocimetry (PIV) and the Optical Current Meter (OCM) techniques (Chickadel et al., 2003; Holland et al., 2001; Puleo et al., 2003) enable surface flow estimates in the surf and swash zones every few m on wave (1 s) and mean current (2 min) time scales (Dooley et al., 2025; McCormack et al., 2025; Muscalus et al., 2025). The PIV and OCM techniques agree well with in situ observations for breaking-wave-driven shallow alongshore flows in the surfzone (Chickadel et al., 2003; Dooley et al., 2025; Wilson et al., 2014), which are roughly uniform with depth (Faria et al., 1998; Henderson et al., 2017), and resolve flow patterns that may be missed by sparse in situ sensors.

However, the number of field observations may be insufficient for training an artificial intelligence model. Moreover, field observations may be noisy owing to environmental conditions and constraints in data collection methods (McCormack et al., 2025). Incorporating the governing equations of fluid dynamics into purely data-driven machine learning models has proven beneficial, leading to enhanced accuracy in solving partial differential equations under weak supervision. This approach, known as Physics-Informed Neural Networks (PINNs; Raissi et al., 2019), has demonstrated promising results in simpler benchmark problems. However, as solution complexity increases, especially in the presence of multiscale phenomena, PINNs face challenges in trainability and predictive accuracy, as demonstrated by numerical studies (Zhu et al., 2019). This difficulty arises from the inherent limitations of neural networks in capturing fine-scale variations within the training data (Wang et al., 2021). Convolutional-based architectures can address this issue by learning spatial hierarchies through convolutional filters, enabling incorporation of both large- and fine-scale variations in the data (LeCun et al., 2010). Integrating physics-based constraints into these models improves their ability to estimate complex data patterns such as fluid dynamics (Geneva & Zabaras, 2020). These architectures can be merged with

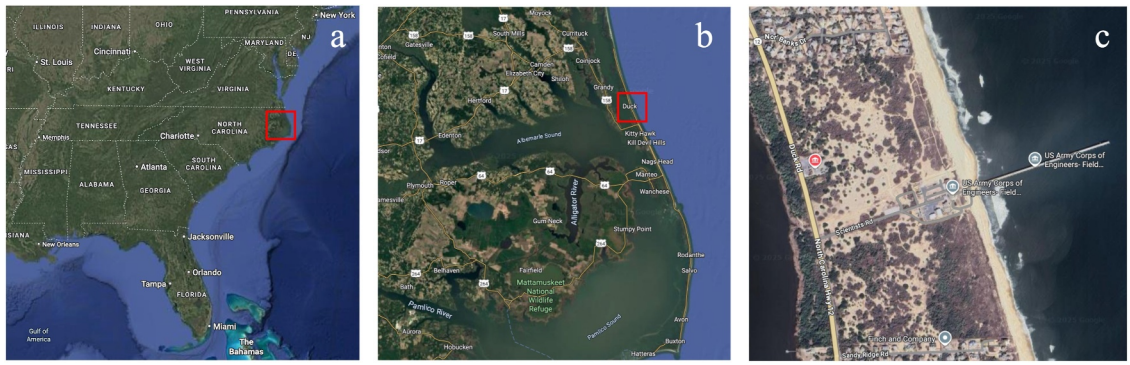

Figure 1. (a) Regional map of the southeastern United States and (b) expanded view of Albemarle and Pamlico Sounds and the adjacent barrier-island coastline with a red box surrounding the study site on the Outer Banks of North Carolina, and (c) the study site at the Field Research Facility in Duck, NC (north toward the top). The pier is ∼500 m long, similar to the width of the island onshore of the pier.

Variational Bayes methods (Kingma & Welling, 2013) to account for predictive uncertainty, an inherent characteristic of field data, and to improve resilience in situations where data are scarce or noisy.

Here, spatially distributed surfzone water depths are estimated using remote-sensing observations of surfzone surface flow fields collected for a range of conditions (Section 2) via a data-driven, physics-informed deep conditional generative model (Section 3). The model is trained to predict water depths from surface flows, and its performance is evaluated under both in-distribution (ID) and out-of-distribution (OOD) scenarios (Section 4). The study concludes with a discussion of findings and future research directions (Section 5).

2. Field Observations

The data set comprises remotely sensed surface flow fields and corresponding water depths (computed as the difference between static bathymetry and time-varying offshore water levels) collected at the US Army Corps of Engineers Field Research Facility (FRF) in Duck, NC (Figure 1), between 2013 and 2022. Measurements span multiple surveys over seven distinct bathymetries (Table 1, B1–B7). For each bathymetry, several 30-min-averaged surface flow-water depth pairs are available, corresponding to different oceanographic conditions.

The model is trained using flow fields as input, with corresponding water depths as output, with true water depths used to compute loss during training. In-distribution (ID) evaluation involves testing the trained model on flow fields from the same bathymetry as used in training, but using different surface flow and water depth pairs. This allows assessment of how well the model generalizes across time-varying ocean forcing, assuming stable bathymetry. In contrast, out-of-distribution (OOD) evaluation tests the model on unseen bathymetry (Table 1, B7), where neither surface flows nor associated water depths were included during training, enabling assessment of generalization across both spatial and temporal variability. For Cases B1-B6 (ID evaluation, Table 1), 25% of the

Table 1
Experiment Cases for the Model

Case	Bathymetry survey date	Video record start time (ET)	30-min flow-depth pairs	Train-test split (%)	$\lvert r \rvert_{\text{within}}$
B1	2013-10-02	(B1-1) 2013-10-01 11:00	12	25–75	0.94
		(B1-2) 2013-10-02 12:00			0.88
B2	2018-09-19	(B2) 2018-09-20 10:00	4	25–75	0.94
B3	2021-08-30	(B3) 2021-08-29 13:00	4	25–75	0.87
B4	2021-09-05	(B4-1) 2021-09-04 09:00	8	25–75	0.91
		(B4-1) 2021-09-04 16:00			0.88
B5	2021-09-07	(B5) 2021-09-08 08:00	8	25–75	0.89
B6	2022-10-07	(B6) 2022-10-08 10:00	4	25–75	0.84
B7	2013-10-22	(B7) 2013-10-20 09:00	18	0–100	0.56

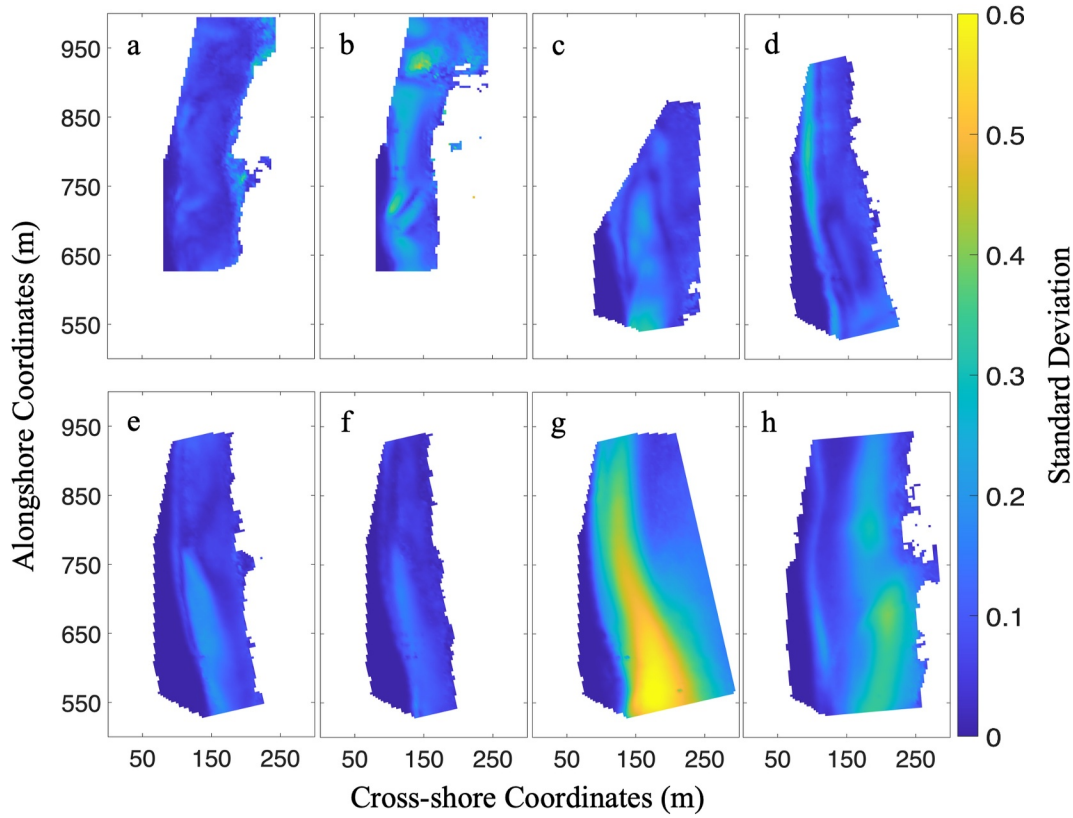

Figure 2. Standard deviation of the flow field (color scale on right) as a function of alongshore and cross-shore coordinates for the Cases (a) B1-1, (b) B1-2, (c) B2, (d) B3, (e) B4-1, (f) B4-2, (g) B5, and (h) B6.

available observed surface flow and water depth pairs were randomly selected for training, with the remainder of surface flows reserved for testing. The 25/75 split (rather than the more typical 80/20) was chosen to test model generalization under realistic data-scarce conditions common at most coastal sites. For Case B7 (OOD evaluation), the trained model is tested on all surface flow fields to infer the corresponding water depths.

Bathymetry from the dry beach to offshore of the surfzone was surveyed during mild conditions with surface vehicles (Forte et al., 2026) that traversed along cross-shore transects separated by 12–45 m in the alongshore. Raw survey data points were spatially interpolated to a 3.2 m grid. The bathymetries ranged from relatively alongshore uniform to complicated seafloors with crescentic sand bars, bumps, and holes (described below).

Surface flows are estimated within 24 hr of the bathymetry surveys by tracking breaking-wave-induced foam with Particle Image Velocimetry (PIV; Raffel et al., 2018) in optical images collected with cameras mounted on a 40-m-tall tower (Dooley et al., 2025; Muscalus et al., 2025). Over a wide range of conditions and locations within the surfzone, correlations (R^2) between ~10 and 60-min mean remotely sensed and in situ estimates were $R^2 = 0.8$ for alongshore currents and $R^2 = 0.5$–0.7 for cross-shore currents (correlations were reduced if there was undertow below the surface) when there was sufficient foam to track, usually for significant wave heights greater than ~0.5 m (Dooley et al., 2025; Muscalus et al., 2025). The nine recordings, which have durations ranging from 120 to 540 min (Table 1), are broken into 30-min periods. The 40 resulting 30-min-averaged surface flow fields over bathymetries B1 through B6 are used for ID training and testing, whereas the 18 30-min-averaged surface flow fields over bathymetry B7 are used to evaluate model predictions on the OOD data set. Gaps in estimated flows occur owing to insufficient foam or lighting conditions (Dooley et al., 2025).

For each case, the standard deviation of the flow field (Figure 2) at each grid point is calculated to quantify flow variability, using flow values from all 30-min flow fields within that case. A higher standard deviation indicates greater variability in flow, resulting in a natural distribution shift between training and testing samples, which helps prevent overfitting and enhances the model's generalization.

10.1029/2025JH000906

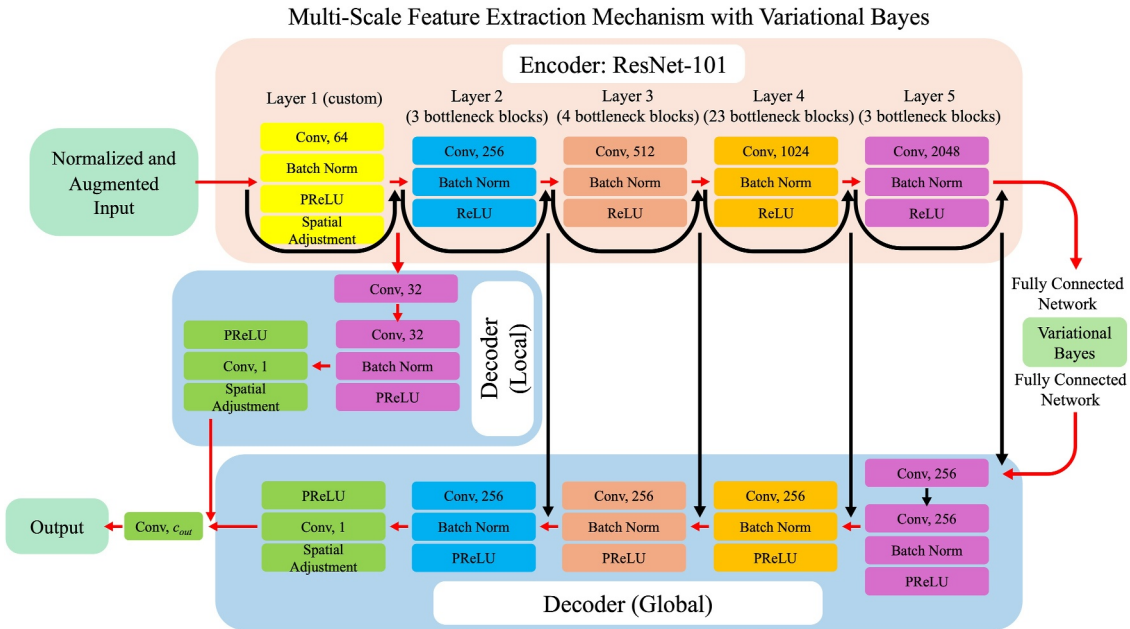

Figure 3. Deep conditional generative model consisting of an encoder with ResNet-101, fully connected networks and latent space, a global decoder, and a local decoder. Skip connections are shown with black arrows.

To investigate the similarities or differences among the flow fields, within-case flow consistency was quantified by computing mean pairwise correlations between individual 30-min flow realizations for each case (Table 1, $|r|_{within}$). Within-case flow correlations for Cases B1–B6 are high ($|r|_{within} > 0.84$), confirming flow consistency over the same bathymetry despite varying conditions. For between-case comparisons, the 30-min remotely sensed estimates of currents for each case were averaged, producing case-averaged flow fields. The correlations of these case-averaged flow fields with each other range from negative to positive (not shown). High correlation values ($|r|_{between} \geq 0.50$, Cohen, 2013) suggest similar flow structures, and thus a model trained on one case may perform well on others with similar patterns, but also could risk overfitting. Lower correlation ($|r|_{between} < 0.30$, Cohen, 2013) indicates distinct flow characteristics, which may challenge model performance on unseen data. For many ID cases (B1–B6) the correlations are moderate (e.g., B2–B4 with B6) to high (e.g., B2 with B4). In contrast, usually the correlations with OOD Case B7 are low, suggesting that a model trained on B1–B6 may struggle to generalize to B7 in OOD evaluation. The high within-case correlations combined with low between-case correlations confirms that the data set contains both sufficient consistency for training and sufficient diversity for meaningful testing.

3. Model Architecture

3.1. Multi-Scale Feature Extraction Mechanism

The estimates of surface flows are on a 3.2 × 3.2 m spatial grid, with 76 cross-and 126 alongshore grid points. The model uses four-dimensional input matrices of 2 × 2 × 76 × 126, which include 2 batches, 2 channels, and the cross- and alongshore grid points including the cross- and alongshore surface flow estimates. These variables are normalized using their extreme values for efficient training (LeCun et al., 2002), followed by data augmentation techniques including flipping, rotation, and noise addition before feeding to the model as a training data set to reduce model overfitting. The model has a single channel for predicted water depth.

The model uses Conditional Variational Autoencoder (CVAE; Sohn et al., 2015) architecture composed of an encoder, a latent space, a global decoder, and a local decoder (Figure 3) in PyTorch (Paszke et al., 2019). The encoder, which is responsible for extracting features (information and patterns) from the input data, uses ResNet-101 (He et al., 2016) as the backbone structure pretrained on the ImageNet data set (Deng et al., 2009). Passing through the encoder layers, each input batch is transformed into feature maps of size 1 × 2048 × 7 × 7 that are flattened to form vectors. Based on the Gaussian distributions of the vectors in pairs of connected layers, 64 means

and log-variances are computed through a differentiable process to form a lower-dimensional "latent space" representation that captures the essential characteristics of the input data. The latent space allows the model to learn and generate meaningful data distributions. The sampled data is passed through a fully connected layer in the global decoder, generating intermediate representations from which it constructs an output tensor through a specific pipeline. Multiple skip connections are included at different stages to facilitate gradient propagation and enhance model performance. The local decoder also constructs an output tensor, and the output tensors from the local and global encoders are fused to form the output water depth estimate.

Despite the complex architecture and aggressive train/test split, model overfitting is mitigated by data augmentation, strong regularization, and physics-based loss constraints. The loss function incorporating regularization and physics-based constraints is detailed in the following section.

3.2. Loss Calculation

The deep conditional generative model is trained by minimizing a total loss function that includes the three components: total variation loss ($\mathcal{L}_{\mathrm{TV}}$), data loss ($\mathcal{L}_{\mathrm{DATA}}$), and residual or physical loss ($\mathcal{L}_{\mathrm{RES}}$). The total variation loss, which smooths the model predictions by reducing differences between neighboring pixel values in the predicted water depth, is defined as:

$$\mathcal{L}_{\mathrm{TV}} = \lambda \sum_{j=1}^{N} \sum_{i=1}^{M} \sqrt{\left(\hat{h}_{i,j+1} - \hat{h}_{i,j}\right)^2 + \left(\hat{h}_{i+1,j} - \hat{h}_{i,j}\right)^2} \tag{1}$$

where λ is a scaling factor (here $\lambda = 0.1$), $\hat{h}$ is the predicted water depth at each grid point, M and N represent the total number of grid points with indices i and j in the cross- and alongshore directions, respectively.

The data loss, which determines the discrepancy between the predicted ($\hat{h}$) and surveyed (h) water depth is composed of both Huber and Kullback-Leibler Divergence (KLD) loss terms:

$$\mathcal{L}_{\mathrm{DATA}} = \frac{1}{L} \sum_{k=1}^{L} \mathrm{Huber}\left(\hat{h}_k, h_k\right) + \mathrm{KLD} \tag{2}$$

where L represents the total number of point measurements with indices k from the grid space for the entire domain. The Huber loss term balances the influence of both large and small errors, ensuring a robust and stable loss function compared with Mean Squared Error (MSE) by transitioning to linear scaling for large residuals, reducing sensitivity to outliers in field data, and is defined as:

$$\mathrm{Huber\ Loss}\left(\hat{h}_k, h_k\right) = \begin{cases} \frac{1}{2}\left(\hat{h}_k - h_k\right)^2 & \text{for } \left|\hat{h}_k - h_k\right| \le \delta \\ \delta.\left(\left|\hat{h}_k - h_k\right| - \frac{1}{2}.\ \delta\right) & \text{otherwise} \end{cases} \tag{3}$$

where δ (here $\delta = 0.1$) determines the transition point between the quadratic and linear regions of the Huber loss function and balances the treatment of small and large errors. The KLD loss term measures the difference between the learned latent distribution and the prior distribution to regularize the latent space so that it has a Gaussian distribution. Without this regularization, the encoder could learn arbitrary representations that the decoder cannot interpret reliably, leading to unstable predictions. Constraining to a Gaussian prior ensures consistent and physically meaningful depth predictions:

$$\mathrm{KLD} = -0.5 \sum_{p=1}^{R} \left(1 + \log\left(\sigma_p^2\right) - \mu_p^2 - \sigma_p^2\right) \tag{4}$$

where R indicates the total number of Gaussian distributions (here $R = 64$), p is the index for each Gaussian distribution, σ^2 denotes the variance, and μ^2 represents the mean of these distributions.

The residual loss, which ensures that the predictions adhere to the physical laws governing the flow motion in the domain, is based on simplified steady-state shallow water equations:

$$\mathcal{L}_{\mathrm{RES}} = \frac{1}{T}\sum_{r=1}^{T} \mathrm{Huber}(\mathrm{RC}_r + \mathrm{RMX}_r + \mathrm{RMY}_r, 0) \tag{5}$$

where T indicates the total number of individual grid points (selected either from within the domain or from its boundaries), with indices r used for calculating the residual loss. The Huber loss is calculated for simplified nonlinear shallow water mass (RC) and momentum balances in the cross- (RMX) and alongshore (RMY) directions, given by:

$$\mathrm{RC}_r = \frac{\partial(\hat{h}_r U_r)}{\partial x} + \frac{\partial(\hat{h}_r V_r)}{\partial y} \tag{6a}$$

$$\mathrm{RMX}_r = \frac{\partial(\hat{h}_r U_r U_r)}{\partial x} + \frac{\partial(\hat{h}_r U_r V_r)}{\partial y} + g\hat{h}_r\frac{\partial \hat{h}_r}{\partial x} \tag{6b}$$

$$\mathrm{RMY}_r = \frac{\partial(\hat{h}_r V_r U_r)}{\partial x} + \frac{\partial(\hat{h}_r V_r V_r)}{\partial y} + g\hat{h}_r\frac{\partial \hat{h}_r}{\partial y} \tag{6c}$$

where U_r and V_r are the cross- and alongshore components of the input surface flow field, g is the gravitational acceleration, and $\frac{\partial}{\partial x}$ and $\frac{\partial}{\partial y}$ indicate spatial derivatives in the cross- and alongshore directions, respectively. Spatial derivatives are computed using second-order centered finite differences for interior grid points and first-order forward/backward differences at domain boundaries, with spatial steps $\Delta x = \Delta y = 3.2$ m determined by the flow field resolution. Grid points with missing data are excluded from the residual loss calculation.

The physics-based training requires that the residual terms (the left side of Equations 6a–6c) are minimized. Temporal fluctuations in water depth within a grid cell are negligible over the 30-min averaged flows, and thus RC_r should be small (non-zero RC_r may occur owing to noisy observations or vertical-flow structure). Many studies have shown a one-dimensional-horizontal balance (1DH) on alongshore uniform beaches with cross-shore wave-driven setup and alongshore bottom stress balancing onshore and diagonal radiation stresses, respectively (Longuet-Higgins & Stewart, 1964, and many field, laboratory, and numerical studies). In contrast, pressure gradients and advection affect alongshore variable flow patterns (Christensen et al., 2025; Hansen et al., 2015; Putrevu et al., 1995), especially at relatively small length scales (<100 m, Wilson et al., 2013). It has been suggested that the wide range of conditions for which the 1DH balances hold is at least partly owing to this cancellation of the 2DH terms. For example, converging feeder currents resulting in cross-shore rips have been parameterized well assuming a balance between pressure gradients and advection along a streamline (Moulton et al., 2017). Here, the "residual" momentum terms (Equation 6b and 6c) that include advection and pressure gradients (neglected in the 1DH balances and that roughly balance on alongshore variable beaches (Wilson et al., 2013)) are used to estimate the local coupling between non-uniform flows and bathymetric features.

Data loss ($\mathcal{L}_{\mathrm{DATA}}$) contributes the largest portion of the total loss (Figure 4a). The residual loss ($\mathcal{L}_{\mathrm{RES}}$) is the second largest term, initially decreasing within the first 1000 epochs before stabilizing. Total variation loss is the smallest component and converges within the first 500 epochs. Training was stopped at 5000 epochs when total loss plateaued (black curve in Figure 4a).

The learning rate, which determines the step size for optimization updates, is adjusted using a cyclic scheduler (Smith, 2017), where the base learning rate is set to 10^{-7} and the maximum learning rate is 10^{-4} (Figure 4b). The learning rate oscillates between the base and maximum learning rates with an amplitude that is reduced by half for each cycle. Compared with a step scheduler, this method results in a more explorative behavior in the model, preventing it from getting trapped in local minima. Additionally, L2 regularization (weight decay = 0.1) is applied to all trainable parameters via the AdamW optimizer (Loshchilov & Hutter, 2019) to prevent overfitting.

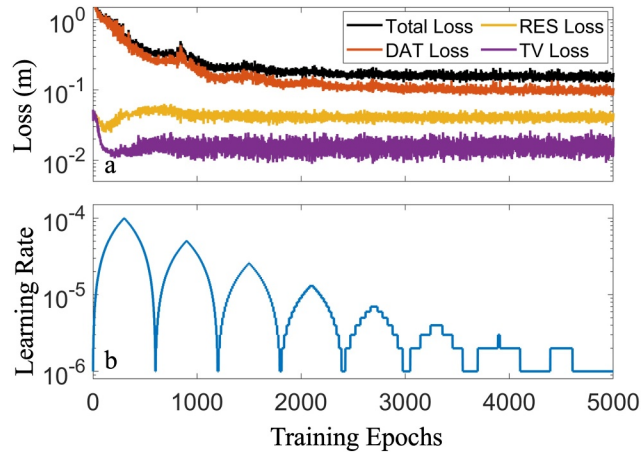

Figure 4. (a) Total (black curve), data (red curve), residual (yellow curve), and total variation (purple curve) losses, and (b) cyclic learning rate versus training epoch for 30-min mean flows.

4. Results

Overall, model predictions (which are constrained to areas with observed flows, Figures 5a–5d and 6a–6d) in ID evaluation agree qualitatively (Figures 5i–5l and 6i–6l) with the surveyed water depths (Figures 5e–5h and 6e–6h), with the difference maps (Figures 5m–5p and 6m–6p) revealing spatial patterns of prediction errors. In Cases B1-1 and B1-2 (first and second columns in Figure 5) both the relatively deep channels (shown inside boxes) are reproduced by the model. In both Case B1-1 and B1-2, the locations of the channels near alongshore coordinates $Y = 700$ (shown with dashed boxes) and 900 m (shown with dash-dot boxes) are reproduced, but there are differences in the details of the modeled water depths. For example, the modeled channel for B1-1 near $Y = 700$ m is deeper than observed (red contours in Figure 5m), and the modeled channel for B1-2 near $Y = 700$ is shallower than observed (blue contours in Figure 5n), possibly owing to differences in the circulation patterns over the same bathymetry. In Case B2, the shallow area observed near $X = 200$ and $Y = 750$ m is reproduced by the model, if somewhat deeper, whereas the bathymetry near $X = 150$ m is predicted to be somewhat deeper than observed (compare the dashed circle in Figure 5k with the dashed circle in Figures 5g and 5o). In Case B3, the overall pattern of the modeled bathymetry is similar to that observed (compare Figures 5l with 5h), although there are quantitative differences (Figure 5p).

For Case B4-1, weak flows at $X = 150$ and $Y = 800$ m (Figure 6a) resulted in a predicted channel that is not observed (compare the dashed circle in Figure 6i with the dashed circle in Figures 6e and 6m). Conversely, in Case B4-2, similarly weak flows (Figure 6b) yield more skillful, though still slightly deeper than observed predictions (compare the dashed circle in Figure 6j with the dashed circle in Figures 6f and 6n). In Case B5 flows are relatively strong and alongshore directed (Figure 6c), the predicted nearshore water depths and the sandbar at $X = 200$ and $Y > 750$ m align well with the survey-derived depths, but the model predicts a more pronounced channel in the central portion than observed (compare the dashed circle in Figure 6k with the dashed circle in Figures 6g and 6o). Furthermore, in the presence of strong alongshore currents (Figure 6c, note that scale arrows in Figures 6c and 6d are twice those in Figures 5 and 6a, 6b) the remote sensing estimates of surface currents underestimate the depth-averaged offshore-directed flows (Dooley et al., 2025), likely leading to errors in modeled water depths when using continuity (Equation 6a) as part of the minimization process. The modeled bathymetry in Case B6, also with strong alongshore currents, but with a more alongshore nonuniform circulation pattern (Figure 6d), is consistent with the observed water depths (compare Figures 6l with 6h and 6p). The location and shape of the sandbar ($X = 150$ m) and the channel across it ($150 < X < 250$ m, $Y = 750$ m, Figures 6h and 6l) are modeled well, although water depths in B6 are shallower than observed (Figure 6p).

Cases B4-1 and B4-2 share the same bathymetry (B4), but differ in water depth and circulation due to tidal stage variation. The currents for the OOD data set Case 7 include spatially varying circulation patterns, and a wide range of both cross- and alongshore flow speeds (Figure 7a). The locations and approximate sizes of the two

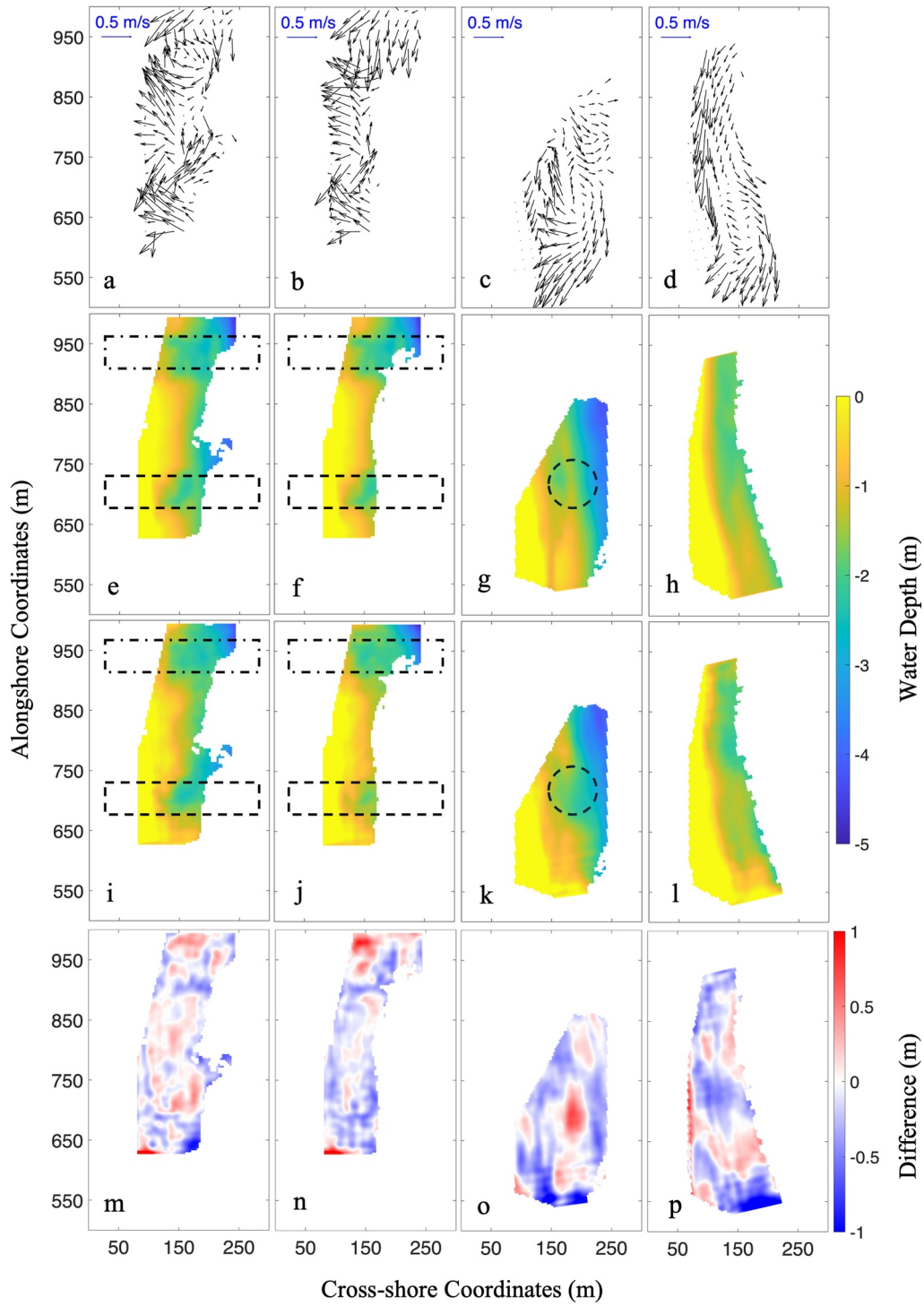

Figure 5. (a–d) Thirty-minute averaged surface flow fields used as model input (every 5th vector shown), (e–h) observed water depths (ground truth), (i–l) model-predicted water depths, and (m–p) differences between observed and model-predicted water depths versus alongshore and cross-shore coordinates for Cases B1-1, B1-2, B2, and B3 (columns 1–4). Cases B1-1 and B1-2 share the same bathymetry (B1), but differ in water depth and circulation due to tidal stage variation.

cross-shore channels (shown with dashed and dashed-dotted rectangles) observed in surveys are reproduced by the model, though with limited accuracy in channel width and depth (compare Figures 7c with 7b). However, overall the predicted water depths are greater than the observed values (Figure 7d).

10.1029/2025JH000906

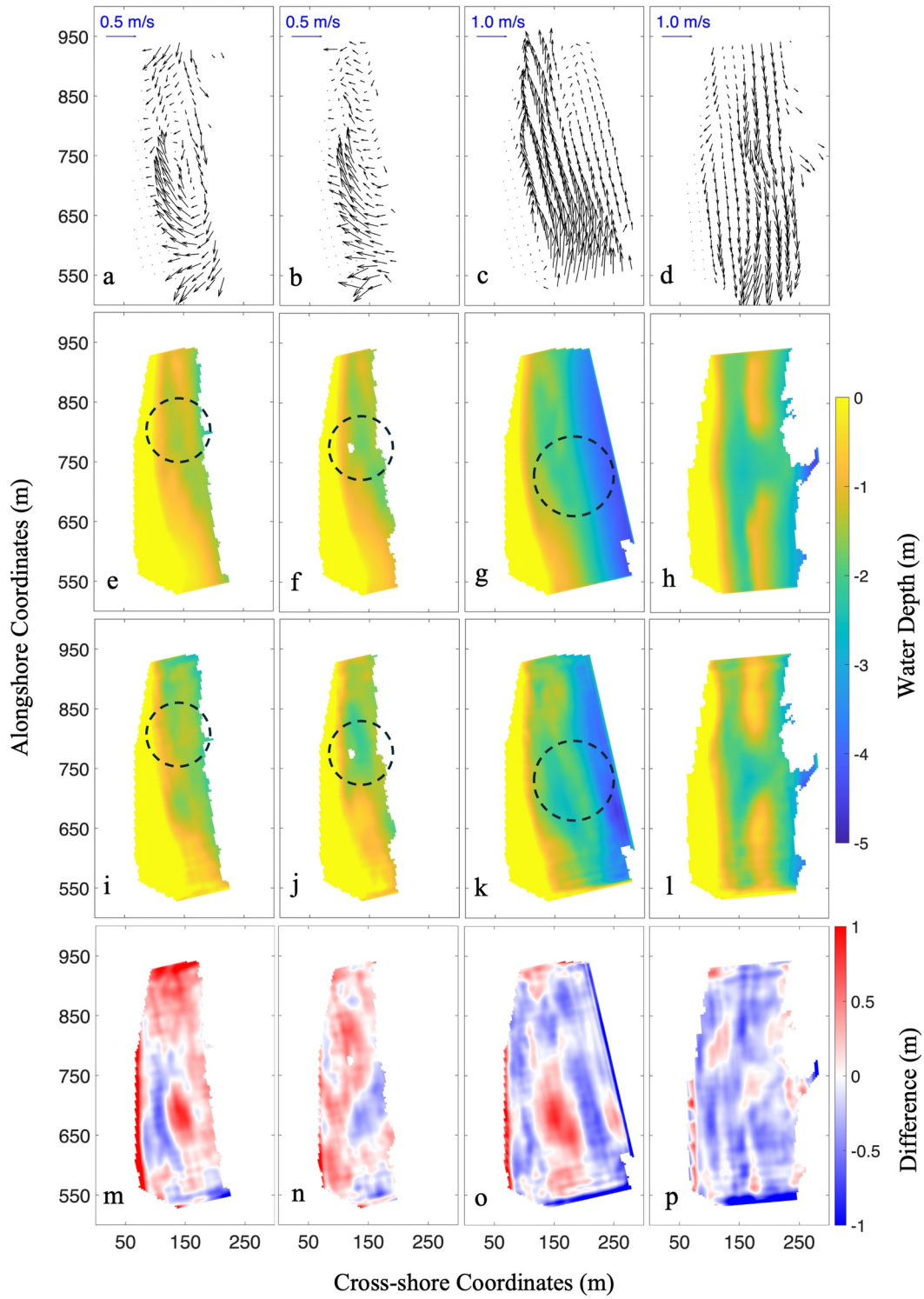

Figure 6. (a–d) Thirty-minute averaged surface flow fields used as model input (every 5th vector shown), (e–h) observed water depths (ground truth), (i–l) model-predicted water depths, and (m–p) differences between observed and model-predicted water depths versus alongshore and cross-shore coordinates for Cases B4-1, B4-2, B5, and B6 (columns 1–4).

For each test case, prediction errors were quantified with RMSE and uncertainty estimated by sampling 100 posterior realizations (Table 2). The RMSE was computed by averaging the 100 posterior samples to obtain mean predictions for each flow realization, calculating spatial errors against observed depths, and averaging squared

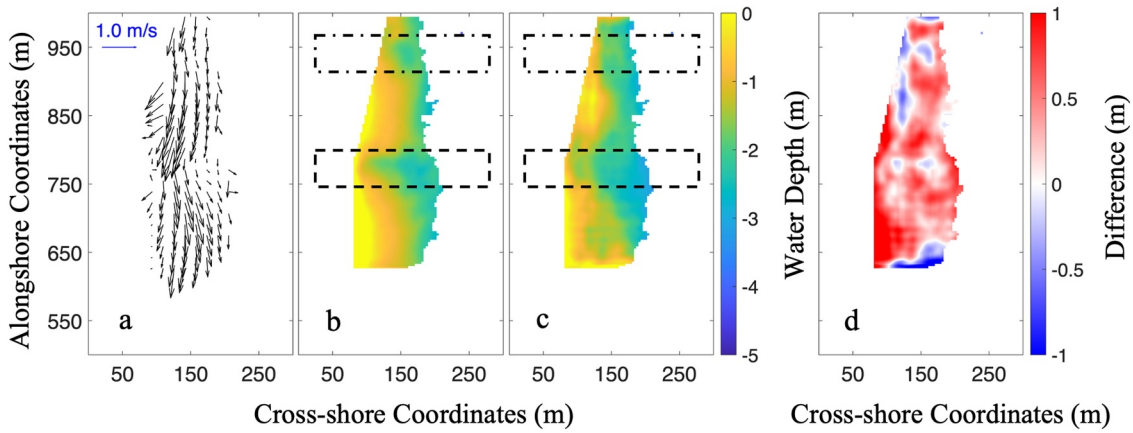

Figure 7. (a) Thirty-minute averaged surface flow fields used as model input (every 5th vector shown), (b) observed water depths (ground truth), (c) model-predicted water depths, and (d) difference between observed and model-predicted water depths, as functions of alongshore and cross-shore coordinates for Case B7.

errors across all grid points and flow realizations within each case. Mean 90% confidence interval width is the average span between 5th and 95th percentiles, where coverage is the percentage of observations within these intervals, averaged across all grid points and flow realizations for each case. The RMSE for ID cases ranges from 0.18 to 0.66 m, with B1-1, B1-2, B2, B3, and B4-2 achieving lower errors (RMSE = 0.18–0.23 m) and higher coverage (81%–90%). The cases B4-1, B5, and B6 show larger errors (RMSE = 0.38–0.50 m) and reduced coverage (52%–70%). The OOD Case B7 has the highest error (RMSE = 0.66 m) and lowest coverage (30%). Confidence limit widths remain constant (∼0.54–0.56 m) across cases. The reduced coverage for challenging cases demonstrates that the model appropriately flags predictions with lower confidence and provides practical value for coastal managers to identify regions requiring additional observations. However, interval widths do not expand proportionally, and thus the model provides relative rather than absolute uncertainty. Coverage values serve as reliability indicators, with coverage below 60% signaling that results may be unreliable. Achieving fully calibrated forecasts where 90% intervals consistently contain 90% of observations requires additional development.

5. Discussion

5.1. Comparison With Existing Methods

The RMSE for the PINN approach used here ranged from 0.18 to 0.66 m (Table 3), comparable with the RMSE obtained using different variants of the wave-celerity approach of cBathy (Lange et al., 2023) (Table 3). For example, different versions of cBathy have RMSE errors in the surfzone from 0.17 (cBathyCT) to 0.81 m (standard cBathy; Table 3). cBathy errors increase with wave heights (Brodie et al., 2018), whereas energetic waves produce strong foam signals allowing better PIV-derived currents (Dooley et al., 2025; Muscalus et al., 2025), and thus more robust estimates of bathymetry. The methods are complementary, with cBathy working well in mild wave conditions when there may be insufficient foam to estimate currents accurately, whereas the surface current estimates and the PINN approach works better in energetic conditions.

5.2. Limitations and Future Improvements

This preliminary study with a limited data set suggests that surfzone bathymetry might be estimated knowing surface currents, which can be obtained remotely. However, to strengthen the influence of physical constraints

Table 2
Domain- and Case-Averaged Errors and Uncertainty Metrics of Model Predictions

Case	B1-1	B1-2	B2	B3	B4-1	B4-2	B5	B6	B7
RMSE (m)	0.23	0.21	0.21	0.22	0.50	0.18	0.38	0.42	0.66
Mean 90% CI Width (m)	0.54	0.54	0.55	0.56	0.56	0.56	0.56	0.55	0.54
Coverage (%)	81	86	87	88	52	90	70	61	30

Table 3
Comparison of Surfzone RMSE for Different Versions of cBathy With the ML Model

Method	Input data	RMSE (m)
Versions of cBathy (Lange et al., 2023)	Optical imagery to estimate wave celerity	0.17–0.81
Present ML model	Optical imagery to estimate surface flows	0.18–0.66

during model training, several factors should be considered. For instance, it remains uncertain whether the mass conservation equation is satisfied by the estimated surface flows, which do not detect mid-water column offshore-directed mean currents (undertow). Similarly, the shallow water equations are based on depth-averaged flows. Surfzone flows may be influenced by wave conditions and topography outside the study region, which means more time could be required for the flows and bathymetry to reach equilibrium. As discussed above, the simplified momentum equations (Equation 6) omit radiation stress gradients assuming they are balanced by setup and bottom stress. Moreover, the data set lacks sufficient in situ observations to estimate the wave frequency-directional spectrum necessary to determine radiation stresses and to estimate setup. Although including observed or modeled wave forcing likely would improve the estimates of bathymetry, the results demonstrate that bathymetric recovery from surface flows alone is feasible.

5.3. Implications for Coastal Monitoring

Bathymetry estimation from surface currents could address a critical gap in nearshore observation systems. Flow-based methods require sufficient foam tracer, which is naturally abundant during energetic conditions when wave celerity methods become less reliable due to pervasive breaking. With increasing availability of shore-mounted cameras for coastal monitoring, the flow-based method could enable continuous and low-cost bathymetric observations resulting in improved understanding of storm-driven morphologic evolution and supporting coastal management decisions.

6. Conclusions

A physics-informed, data-driven deep conditional generative model is shown to predict surfzone water depths (bathymetry) at least qualitatively from remotely sensed surface flows, even with a strongly limited set of training data (6 bathymetries with a total of 8 flow fields). The model leverages a composite loss function that integrates data, physical, and total variation losses to enhance predictive accuracy. It is trained on 25% of in-distribution (ID) data sets and tested on the remaining 75%, as well as on out-of-distribution (OOD) data sets. Domain- and case-averaged Root Mean Square Errors (RMSE) ranged from 0.18 to 0.50 for ID cases and was 0.66 m for the OOD cases.

Conflict of Interest

The authors declare no conflicts of interest relevant to this study.

Data Availability Statement

High-spatial resolution survey can be found here: (Elgar & Raubenheimer, 2019), and the other surveys and offshore wave conditions can be found on the FRF THREDDS server (U.S. Army Corps of Engineers, Coastal and Hydraulics Laboratory, 2026). The remote sensing data are available at (Dooley et al., 2024). Model training code is available at (Salatin et al., 2025).

Acknowledgments
We thank the PVLAB and FRF field crews for obtaining observations in sometimes difficult surfzone conditions, Ciara Dooley, Alex Muscalus, and Levi Gorrell for their remote sensing expertise, and the National Science Foundation for funding.

References

Adusumilli, S., Cirrito, N., Engeman, L., Fiedler, J. W., Guza, R. T., Lange, A. M., et al. (2024). Predicting shoreline changes along the California coast using deep learning applied to satellite observations. *Journal of Geophysical Research: Machine Learning and Computation*, *1*(3), e2024JH000172. https://doi.org/10.1029/2024jh000172

Birkemeier, W. A., & Mason, C. (1984). The CRAB: A unique nearshore surveying vehicle. *Journal of Surveying Engineering*, *110*(1), 1–7. https://doi.org/10.1061/(asce)0733-9453(1984)110:1(1)

Birrien, F., Castelle, B., Marieu, V., & Dubarbier, B. (2013). On a data-model assimilation method to inverse wave-dominated beach bathymetry using heterogeneous video-derived observations. *Ocean Engineering*, *73*, 126–138. https://doi.org/10.1016/j.oceaneng.2013.08.002

Blenkinsopp, C. E., Turner, I. L., Allis, M. J., Peirson, W. L., & Garden, L. E. (2012). Application of LiDAR technology for measurement of time-varying free-surface profiles in a laboratory wave flume. *Coastal Engineering*, *68*, 1–5. https://doi.org/10.1016/j.coastaleng.2012.04.006

Brodie, K. L., Palmsten, M. L., Hesser, T. J., Dickhudt, P. J., Raubenheimer, B., Ladner, H., & Elgar, S. (2018). Evaluation of video-based linear depth inversion performance and applications using altimeters and hydrographic surveys in a wide range of environmental conditions. *Coastal Engineering*, *136*, 147–160. https://doi.org/10.1016/j.coastaleng.2018.01.003

Brodie, K. L., Raubenheimer, B., Elgar, S., Slocum, R. K., & McNinch, J. E. (2015). Lidar and pressure measurements of inner-surfzone waves and setup. *Journal of Atmospheric and Oceanic Technology*, *32*(10), 1945–1959. https://doi.org/10.1175/jtech-d-14-00222.1

Castelle, B., Bujan, S., Ferreira, S., & Dodet, G. (2017). Foredune morphological changes and beach recovery from the extreme 2013/2014 winter at a high-energy sandy coast. *Marine Geology*, *385*, 41–55. https://doi.org/10.1016/j.margeo.2016.12.006

Chen, Q., Wang, N., & Chen, Z. (2023). Simultaneous mapping of nearshore bathymetry and waves based on physics-informed deep learning. *Coastal Engineering*, *183*, 104337. https://doi.org/10.1016/j.coastaleng.2023.104337

Chickadel, C. C., Holman, R. A., & Freilich, M. H. (2003). An optical technique for the measurement of longshore currents. *Journal of Geophysical Research*, *108*(C11). https://doi.org/10.1029/2003jc001774

Christensen, D., Raubenheimer, B., & Elgar, S. (2025). The impact of outer-bar alongshore variability on inner-bar rip dynamics. *Earth Surface Processes and Landforms*, *50*(6), e70086. https://doi.org/10.1002/esp.70086

Cohen, J. (2013). *Statistical power analysis for the behavioral sciences* (p. 579). Routledge.

Collins, A. M., Brodie, K. L., Bak, A. S., Hesser, T. J., Farthing, M. W., Lee, J., & Long, J. W. (2020). Bathymetric inversion and uncertainty estimation from synthetic surf-zone imagery with machine learning. *Remote Sensing*, *12*(20), 3364. https://doi.org/10.3390/rs12203364

Collins, A. M., Geheran, M. P., Hesser, T. J., Bak, A. S., Brodie, K. L., & Farthing, M. W. (2021). Development of a fully convolutional neural network to derive surf-zone bathymetry from close-range imagery of waves in Duck, NC. *Remote Sensing*, *13*(23), 4907. https://doi.org/10.3390/rs13234907

Deng, J., Dong, W., Socher, R., Li, L. J., Li, K., & Fei-Fei, L. (2009). Imagenet: A large-scale hierarchical image database. In *2009 IEEE conference on computer vision and pattern recognition* (pp. 248–255).

de Swart, R. L., Ribas, F., Simarro, G., Guillén, J., & Calvete, D. (2021). The role of bathymetry and directional wave conditions on observed crescentic bar dynamics. *Earth Surface Processes and Landforms*, *46*(15), 3252–3270. https://doi.org/10.1002/esp.5233

Di Leonardo, D., & Ruggiero, P. (2015). Regional scale sandbar variability: Observations from the US Pacific Northwest. *Continental Shelf Research*, *95*, 74–88. https://doi.org/10.1016/j.csr.2014.12.012

Dooley, C., Elgar, S., & Raubenheimer, B. (2024). PVLAB: Remotely sensed surface currents from field experiments (2013, 2018, 2021, 2022). https://doi.org/10.5281/zenodo.11581091

Dooley, C., Elgar, S., Raubenheimer, B., & Gorrell, L. (2025). Estimating surfzone currents with near-field optical remote sensing. *Journal of Atmospheric and Oceanic Technology*, *42*(1), 33–46. https://doi.org/10.1175/jtech-d-24-0015.1

Dugan, J. P., Morris, W. D., Vierra, K. C., Piotrowski, C. C., Farruggia, G. J., & Campion, D. C. (2001). Jetski-based nearshore bathymetric and current survey system. *Journal of Coastal Research*, 900–908.

Dugan, J. P., Suzukawa, H. H., Forsyth, C. P., & Farber, M. S. (1996). Ocean wave dispersion surface measured with airborne IR imaging system. *IEEE Transactions on Geoscience and Remote Sensing*, *34*(5), 1282–1284. https://doi.org/10.1109/36.536544

Elgar, S., & Raubenheimer, B. (2019). Surf zone vorticity and advection (RODSEX) field experiment, DesignSafe-CI. https://doi.org/10.17603/ds2-c9p4-7264

Ellenson, A. N., Simmons, J. A., Wilson, G. W., Hesser, T. J., & Splinter, K. D. (2020). Beach state recognition using argus imagery and convolutional neural networks. *Remote Sensing*, *12*(23), 3953. https://doi.org/10.3390/rs12233953

Faria, A. G., Thornton, E. B., Stanton, T. P., Soares, C. K., & Lippmann, T. C. (1998). Vertical profiles of longshore currents and related bed shear stress and bottom roughness. *Journal of Geophysical Research*, *103*(C2), 3217–3232. https://doi.org/10.1029/97jc02265

Forte, M., Gorrell, L., Elgar, S., Raubenheimer, B., Dickhudt, P., & Mitchell, J. (2026). Evaluation of surfzone survey systems during calm and rough sea states. *Journal of Surveying Engineering*, *152*(2), 04025021. https://doi.org/10.1061/JSUED2.SUENG-1645

Francis, H., & Traykovski, P. (2021). Development of a highly portable unmanned surface vehicle for surf zone bathymetric surveying. *Journal of Coastal Research*, *37*(5), 933–945. https://doi.org/10.2112/jcoastres-d-20-00143.1

Geneva, N., & Zabaras, N. (2020). Modeling the dynamics of PDE systems with physics-constrained deep auto-regressive networks. *Journal of Computational Physics*, *403*, 109056. https://doi.org/10.1016/j.jcp.2019.109056

Guedes, R. M., Calliari, L. J., Holland, K. T., Plant, N. G., Pereira, P. S., & Alves, F. N. (2011). Short-term sandbar variability based on video imagery: Comparison between time–average and time–variance techniques. *Marine Geology*, *289*(1–4), 122–134. https://doi.org/10.1016/j.margeo.2011.09.015

Haller, M. C., Honegger, D., & Catalan, P. A. (2014). Rip current observations via marine radar. *Journal of Waterway, Port, Coastal, and Ocean Engineering*, *140*(2), 115–124. https://doi.org/10.1061/(asce)ww.1943-5460.0000229

Hansen, J. E., Raubenheimer, B., List, J. H., & Elgar, S. (2015). Modeled alongshore circulation and force balances onshore of a submarine canyon. *Journal of Geophysical Research: Oceans*, *120*(3), 1887–1903. https://doi.org/10.1002/2014jc010555

He, K., Zhang, X., Ren, S., & Sun, J. (2016). Deep residual learning for image recognition. In *Proceedings of the IEEE conference on computer vision and pattern recognition* (pp. 770–778).

Henderson, S. M., Arnold, J., Özkan-Haller, H. T., & Solovitz, S. A. (2017). Depth dependence of nearshore currents and eddies. *Journal of Geophysical Research: Oceans*, *122*(11), 9004–9031. https://doi.org/10.1002/2016jc012349

Holland, K. T., Puleo, J. A., & Kooney, T. N. (2001). Quantification of swash flows using video-based particle image velocimetry. *Coastal Engineering*, *44*(2), 65–77. https://doi.org/10.1016/s0378-3839(01)00022-9

Holman, R., & Bergsma, E. W. (2021). Updates to and performance of the cbathy algorithm for estimating nearshore bathymetry from remote sensing imagery. *Remote Sensing*, *13*(19), 3996. https://doi.org/10.3390/rs13193996

Holman, R., Plant, N., & Holland, T. (2013). cBathy: A robust algorithm for estimating nearshore bathymetry. *Journal of Geophysical Research: Oceans*, *118*(5), 2595–2609. https://doi.org/10.1002/jgrc.20199

Honegger, D. A., Haller, M. C., & Holman, R. A. (2019). High-resolution bathymetry estimates via X-band marine radar: 1. Beaches. *Coastal Engineering*, *149*, 39–48. https://doi.org/10.1016/j.coastaleng.2019.03.003

Janowski, L., Wroblewski, R., Rucinska, M., Kubowicz-Grajewska, A., & Tysiac, P. (2022). Automatic classification and mapping of the seabed using airborne LiDAR bathymetry. *Engineering Geology*, *301*, 106615. https://doi.org/10.1016/j.enggeo.2022.106615

Kabir, S., Patidar, S., Xia, X., Liang, Q., Neal, J., & Pender, G. (2020). A deep convolutional neural network model for rapid prediction of fluvial flood inundation. *Journal of Hydrology*, *590*, 125481. https://doi.org/10.1016/j.jhydrol.2020.125481

Kingma, D. P., & Welling, M. (2013). Auto-encoding variational bayes. *arXiv preprint arXiv:1312.6114*.

Lange, A. M., Fiedler, J. W., Merrifield, M. A., & Guza, R. T. (2023). UAV video-based estimates of nearshore bathymetry. *Coastal Engineering*, *185*, 104375. https://doi.org/10.1016/j.coastaleng.2023.104375

LeCun, Y., Bottou, L., Orr, G. B., & Müller, K. R. (2002). Efficient backprop. In *Neural networks: Tricks of the trade* (pp. 9–50). Springer Berlin Heidelberg.

LeCun, Y., Kavukcuoglu, K., & Farabet, C. (2010). Convolutional networks and applications in vision. In *Proceedings of 2010 IEEE international symposium on circuits and systems* (pp. 253–256).

Lewis, J. M., Lakshmivarahan, S., & Dhall, S. (2006). *Dynamic data assimilation: A least squares approach* (Vol. 13). Cambridge University Press.

Liang, Y., Li, X., Tsai, B., Chen, Q., & Jafari, N. (2023). V-FloodNet: A video segmentation system for urban flood detection and quantification. *Environmental Modelling & Software*, *160*, 105586. https://doi.org/10.1016/j.envsoft.2022.105586

Lillesand, T., Kiefer, R. W., & Chipman, J. (2015). *Remote sensing and image interpretation*. John Wiley & Sons.

Lippmann, T. C., & Holman, R. A. (1990). The spatial and temporal variability of sand bar morphology. *Journal of Geophysical Research*, *95*(C7), 11575–11590. https://doi.org/10.1029/jc095ic07p11575

Longuet-Higgins, M. S., & Stewart, R. W. (1964). Radiation stresses in water waves; a physical discussion, with applications. In *Deep sea research and oceanographic abstracts* (Vol. 11(4), pp. 529–562). Elsevier. https://doi.org/10.1016/0011-7471(64)90001-4

Loshchilov, I., & Hutter, F. (2019). Decoupled weight decay regularization. In *Proceedings of the international conference on learning representations*.

Lowell, K., & Calder, B. (2021). Extracting shallow-water bathymetry from LiDAR point clouds using pulse attribute data: Merging density-based and machine learning approaches. *Marine Geodesy*, *44*(4), 259–286. https://doi.org/10.1080/01490419.2021.1925790

MacMahan, J. H., Thornton, E. B., & Reniers, A. J. (2006). Rip current review. *Coastal Engineering*, *53*(2–3), 191–208. https://doi.org/10.1016/j.coastaleng.2005.10.009

Martins, K., Brodie, K. L., Fiedler, J. W., O'dea, A. M., Spore, N. J., Grenzeback, R. L., et al. (2025). Seamless nearshore topo-bathymetry reconstruction from LiDAR scanners: A proof-of-concept based on a dedicated field experiment at Duck, NC. *Coastal Engineering*, *199*, 104748. https://doi.org/10.1016/j.coastaleng.2025.104748

McCormack, T., Hopkins, J., Raubenheimer, B., Elgar, S., & Brodie, K. L. (2025). Remote sensing of wave-orbital velocities in the surfzone. *Coastal Engineering*, *195*, 104631. https://doi.org/10.1016/j.coastaleng.2024.104631

Moulton, M., Elgar, S., Raubenheimer, B., Warner, J. C., & Kumar, N. (2017). Rip currents and alongshore flows in single channels dredged in the surf zone. *Journal of Geophysical Research: Oceans*, *122*(5), 3799–3816. https://doi.org/10.1002/2016jc012222

Muñoz, D. F., Muñoz, P., Moftakhari, H., & Moradkhani, H. (2021). From local to regional compound flood mapping with deep learning and data fusion techniques. *Science of the Total Environment*, *782*, 146927. https://doi.org/10.1016/j.scitotenv.2021.146927

Muscalus, A., Elgar, S., Raubenheimer, B., Gorrell, L., & Dooley, C. (2025). Field observations of swash zone currents estimated with near field optical remote sensing. *Journal of Atmospheric and Oceanic Technology*, *42*(8), 965–977. https://doi.org/10.1175/JTECH-D-24-0156.1

O'Dea, A., Anderson, D., Holman, R., Painter, C., & Brodie, K. (2025). Wave kinematics-based bathymetry estimates from satellite optical video. *Coastal Engineering*, *200*, 104753. https://doi.org/10.1016/j.coastaleng.2025.104753

Palmer, K., Watson, C. S., Power, H. E., & Hunter, J. R. (2024). Quantifying the mean sea level, tide, and surge contributions to changing coastal high water levels. *Journal of Geophysical Research: Oceans*, *129*(8), e2023JC020737. https://doi.org/10.1029/2023jc020737

Paszke, A., Gross, S., Massa, F., Lerer, A., Bradbury, J., Chanan, G., & Chintala, S. (2019). Pytorch: An imperative style, high-performance deep learning library. *Advances in Neural Information Processing Systems*, *32*.

Phillips, B. T., Brown, J. M., Bidlot, J. R., & Plater, A. J. (2017). Role of beach morphology in wave overtopping hazard assessment. *Journal of Marine Science and Engineering*, *5*(1), 1. https://doi.org/10.3390/jmse5010001

Phillips, M. S., Harley, M. D., Turner, I. L., Splinter, K. D., & Cox, R. J. (2017). Shoreline recovery on wave-dominated sandy coastlines: The role of sandbar morphodynamics and nearshore wave parameters. *Marine Geology*, *385*, 146–159. https://doi.org/10.1016/j.margeo.2017.01.005

Plant, N. G., & Holman, R. A. (1999). Extracting morphologic information from field data. In *Coastal engineering 1998* (pp. 2773–2784).

Puleo, J. A., Farquharson, G., Frasier, S. J., & Holland, K. T. (2003). Comparison of optical and radar measurements of surf and swash zone velocity fields. *Journal of Geophysical Research*, *108*(C3). https://doi.org/10.1029/2002jc001483

Putrevu, U., Oltman-Shay, J., & Svendsen, I. A. (1995). Effect of alongshore nonuniformities on longshore current predictions. *Journal of Geophysical Research*, *100*(C8), 16119–16130. https://doi.org/10.1029/95jc01459

Raffel, M., Willert, C. E., Scarano, F., Kähler, C. J., Wereley, S. T., & Kompenhans, J. (2018). *Particle image velocimetry: A practical guide*. Springer.

Raissi, M., Perdikaris, P., & Karniadakis, G. E. (2019). Physics-informed neural networks: A deep learning framework for solving forward and inverse problems involving nonlinear partial differential equations. *Journal of Computational Physics*, *378*, 686–707. https://doi.org/10.1016/j.jcp.2018.10.045

Robertson, Q., Dunkin, L., Dong, Z., Wozencraft, J., & Zhang, K. (2018). Florida and US east coast beach change metrics derived from LiDAR data utilizing ArcGIS Python based tools. *Beach Management Tools-Concepts, Methodologies and Case Studies*, 239–258. https://doi.org/10.1007/978-3-319-58304-4_12

Ruessink, B. G., Coco, G., Ranasinghe, R., & Turner, I. L. (2007). Coupled and noncoupled behavior of three-dimensional morphological patterns in a double sandbar system. *Journal of Geophysical Research*, *112*(C7). https://doi.org/10.1029/2006jc003799

Ruessink, B. G., Pape, L., & Turner, I. L. (2009). Daily to interannual cross-shore sandbar migration: Observations from a multiple sandbar system. *Continental Shelf Research*, *29*(14), 1663–1677. https://doi.org/10.1016/j.csr.2009.05.011

Ruggiero, P., Kaminsky, G. M., Gelfenbaum, G., & Voigt, B. (2005). Seasonal to interannual morphodynamics along a high-energy dissipative littoral cell. *Journal of Coastal Research*, *21*(3), 553–578. https://doi.org/10.2112/03-0029.1

Salatin, R., Chen, Q., Raubenheimer, B., Elgar, S., Gorrell, L., & Li, X. (2024). A new framework for quantifying alongshore variability of swash motion using fully convolutional networks. *Coastal Engineering*, *192*, 104542. https://doi.org/10.1016/j.coastaleng.2024.104542

Salatin, R., Elgar, S., & Raubenheimer, B. (2025). Code for surfzone water depth estimation from surface flows using a data-driven and physics-informed deep conditional generative model. https://doi.org/10.5281/zenodo.18063012

Salim, A., & Wilson, G. (2021). Validation and analysis of a 1-D variational assimilation scheme for bathymetry inversion. *Coastal Engineering*, *167*, 103895. https://doi.org/10.1016/j.coastaleng.2021.103895

Sallenger, A., Wright, C. W., & Lillycrop, J. (2007). Coastal-change impacts during Hurricane Katrina: An overview. *Coastal Sediments' 07*, 888–896. https://doi.org/10.1061/40926(239)68

Sallenger, A. H., Stockdon, H. F., Fauver, L., Hansen, M., Thompson, D., Wright, C. W., & Lillycrop, J. (2006). Hurricanes 2004: An overview of their characteristics and coastal change. *Estuaries and Coasts*, *29*(6), 880–888. https://doi.org/10.1007/bf02798647

Sallenger, A. H., Wright, C. W., Guy, K., & Morgan, K. (2004). Assessing storm-induced damage and dune erosion using airborne lidar: Examples from Hurricane Isabel. *Shore and Beach*, *72*(2), 3–7.

Sallenger, A. H. Jr. (2000). Storm impact scale for barrier islands. *Journal of Coastal Research*, 890–895.

Sallenger, A. H. Jr., Wright, C. W., & Lillycrop, J. (2005). Coastal impacts of the 2004 hurricanes measured with airborne LiDAR: Initial results. *Shore and Beach*, *73*(2), 10–15.

Smith, L. N. (2017). Cyclical learning rates for training neural networks. In *2017 IEEE winter conference on applications of computer vision (WACV)* (pp. 464–472).

Sohn, K., Lee, H., & Yan, X. (2015). Learning structured output representation using deep conditional generative models. *Advances in Neural Information Processing Systems*, *28*.

Thornton, E. B., MacMahan, J., & Sallenger Jr, A. H. (2007). Rip currents, mega-cusps, and eroding dunes. *Marine Geology*, *240*(1–4), 151–167. https://doi.org/10.1016/j.margeo.2007.02.018

U.S. Army Corps of Engineers, Coastal and Hydraulics Laboratory. (2026). Field Research Facility (FRF) THREDDS data server. Retrieved from https://chldata.erdc.dren.mil/thredds/catalog/frf/catalog.html

Van Dongeren, A., Plant, N., Cohen, A., Roelvink, D., Haller, M. C., & Catalán, P. (2008). Beach Wizard: Nearshore bathymetry estimation through assimilation of model computations and remote observations. *Coastal Engineering*, *55*(12), 1016–1027. https://doi.org/10.1016/j.coastaleng.2008.04.011

Van Enckevort, I. M. J., & Ruessink, B. G. (2001). Effect of hydrodynamics and bathymetry on video estimates of nearshore sandbar position. *Journal of Geophysical Research*, *106*(C8), 16969–16979. https://doi.org/10.1029/1999jc000167

Vidal-Ruiz, J. A., & de Alegría-Arzaburu, A. R. (2020). Modes of onshore sandbar migration at a single-barred and swell-dominated beach. *Marine Geology*, *426*, 106222. https://doi.org/10.1016/j.margeo.2020.106222

Wang, N., Chen, Q., & Chen, Z. (2022). Reconstruction of nearshore wave fields based on physics-informed neural networks. *Coastal Engineering*, *176*, 104167. https://doi.org/10.1016/j.coastaleng.2022.104167

Wang, S., Wang, H., & Perdikaris, P. (2021). On the eigenvector bias of Fourier feature networks: From regression to solving multi-scale PDEs with physics-informed neural networks. *Computer Methods in Applied Mechanics and Engineering*, *384*, 113938. https://doi.org/10.1016/j.cma.2021.113938

Wilson, G., & Berezhnoy, S. (2018). Surfzone state estimation, with applications to quadcopter-based remote sensing data. *Journal of Atmospheric and Oceanic Technology*, *35*(10), 1881–1896. https://doi.org/10.1175/jtech-d-17-0205.1

Wilson, G. W., Özkan-Haller, H. T., & Holman, R. A. (2013). Quantifying the length-scale dependence of surf zone advection. *Journal of Geophysical Research: Oceans*, *118*(5), 2393–2407. https://doi.org/10.1002/jgrc.20190

Wilson, G. W., Özkan-Haller, H. T., Holman, R. A., Haller, M. C., Honegger, D. A., & Chickadel, C. C. (2014). Surf zone bathymetry and circulation predictions via data assimilation of remote sensing observations. *Journal of Geophysical Research: Oceans*, *119*(3), 1993–2016. https://doi.org/10.1002/2013jc009213

Wright, L. D., & Short, A. D. (1984). Morphodynamic variability of surf zones and beaches: A synthesis. *Marine Geology*, *56*(1–4), 93–118. https://doi.org/10.1016/0025-3227(84)90008-2

Wu, J., Hao, X., Li, T., & Shen, L. (2023). Adjoint-based high-order spectral method of wave simulation for coastal bathymetry reconstruction. *Journal of Fluid Mechanics*, *972*, A41. https://doi.org/10.1017/jfm.2023.733

Zhu, Y., Zabaras, N., Koutsourelakis, P. S., & Perdikaris, P. (2019). Physics-constrained deep learning for high-dimensional surrogate modeling and uncertainty quantification without labeled data. *Journal of Computational Physics*, *394*, 56–81. https://doi.org/10.1016/j.jcp.2019.05.024